Status and imaging performance of Lowell Observatory's Discovery Channel Telescope in its first year of full science operations

Stephen E. Levine[a,*], William T. DeGroff[a]

[a]Lowell Observatory, 1400 West Mars Hill Road, Flagstaff, AZ 86001, USA

ABSTRACT

Lowell Observatory's Discovery Channel Telescope (DCT) is a 4.3-m telescope designed and constructed for optical and near infrared astronomical observation. The DCT is equipped with a cube capable of carrying five instruments along with the wave front sensing and guider systems at the f/6.1 RC focus. The facility formally finished commissioning at the end of 2014. In 2015 the DCT ran in full science operations mode. This report recaps recent progress on the operations and instrument fronts, and then concentrates on the delivered image quality as measured with science imaging data. The system is delivering image quality at or better than the system top level requirements for open loop operations. Corrected to the zenith, the median seeing in the science images from 2015 was $0.''93$; first quartile seeing was $0.''74$. The open loop site contribution to the seeing is roughly $0.''40$, which is better than the requirements of $< 0.''47$. The FWHM degrades with wind speed at the rate of roughly $0.''10/(m/s)$, and the seeing degrades more with wind speed when the wind is from the East.

Keywords: DCT, Discovery Channel Telescope, Lowell Observatory, System Status, Delivered Image Quality

1. INTRODUCTION

The year 2015 was the first year of full time science operations for Lowell Observatory's 4.3-meter Discovery Channel Telescope (DCT). This contribution provides a brief recap of the project status in §§ 1 and 2 (including pointers to more detailed descriptions of current and upcoming instrumentation), and then focuses primarily on the delivered image quality as derived from science images in §§ 3 and 4. Highlights from 2015 included first light on DCT of both the DeVeny optical spectrograph and the Near IR High Throughput Spectrogragh (NIHTS), and the introduction of regularly supported remote observing.

See Ref. 1 for an overview of the basic site and facility parameters, and Refs. 1, 2 for initial performance assessments. Since the first tentative science nights, DCT has moved in a reasonably straightforward progression into full science operations. In 2013, we scheduled 90.5 nights; in 2014 we scheduled 215.0 nights for science. 2015 was the first year of formal full science operations; that year we scheduled 275.5 nights of science on 293 nights. Nominal full operations is 300 nights per year for science.

The conception of what is now the DCT dates back over two decades. Ground breaking at the Happy Jack, AZ site took place in July 12, 2005. Just over six years later on August 15, 2011, the primary mirror was installed. On sky testing of the major subsystems began on September 1, 2011. The secondary mirror was installed on January 20, 2012, and commissioning work continued, leading up to first light in late spring of 2012. Early, limited science operations for Lowell and its partner institutions, Boston University, the University of Maryland, and the University of Toledo, began in the first quarter of 2013. The commissioning phase was finished at the end of 2014, and the DCT went into full time science operations on January 1, 2015. During that time, the partnership increased to include Northern Arizona University, and Yale University, and we are also working with the University of Texas at Austin and the Korean Astronomy and Space Science Institute (KASI).

Operationally, the telescope is scheduled in half nights. This has provided additional flexibility above whole night classical scheduling. The first demonstration night of remote observing was 2014 March 22 UT. Remote observation has been supported as a general option since the beginning of 2015, limited only by the availability of

---

[*]Corresponding author: E-mail: sel@lowell.edu

a second telescope operator (TO; for on-site safety reasons). Remote observing makes use of industry standard tools: VPN to access the telescope network, and VNC to replicate the observing computer screens to the observers home computer. Communications with the on-site staff is usually over Skype.

2. INSTRUMENTATION RECAP

During the past year, in addition to work completing the first generation instruments (DeVeny and NIHTS), significant work has gone into expanding the available guiding modes. The system is now capable of guiding (i) at sidereal rate, (ii) at constant non-sidereal rates, (iii) while tracking to an object ephemeris, (iv) with the instrument rotator fixed (for example for guiding at the parallactic angle for spectroscopy) and (v) across pointing dithers.

2.1 First Generation Instruments – LMI, DeVeny and NIHTS

The design for the DCT included a Cassegrain instrument cube capable of carrying up to five instruments,[3] in addition to two guider and wave front sensor probes and the low power corrector optics for the straight through beam. The first light instrument was an imaging camera borrowed from the Lowell 42-inch telescope. This was replaced in short order with the first of the planned instruments, the Large Monolithic Imager (LMI). That has been joined by the DeVeny Optical Spectrograph and the Near IR High Throughput Spectrograph (NIHTS), rounding out the initial suite of instruments (these are all discussed in more detail in Ref 4).

The Large Monolithic Imager was installed on DCT in the fall of 2012 and has become a workhorse instrument. The detector is an e2v CCD231 $6.1K \times 6.1K$ CCD, with 15μm square pixels, and the on-sky field of view is $12\overset{\prime}{.}3 \times 12\overset{\prime}{.}3$.[4] P. Massey was the instrument PI. Typically the instrument is used with 2×2 binning, for an effective pixel size of $0\overset{\prime\prime}{.}24$ which is a reasonable match to the typical seeing (see discussion below). Under the best of conditions, and when extra dynamic range is needed, the camera is used unbinned.

To provide optical spectroscopy capability, we upgraded the existing DeVeny spectrograph (the old KPNO white spectrograph) from the Lowell 1.8-meter to the DCT.[4] This required new re-imaging optics and instrument mounting hardware; the upgrade included a new deep depletion CCD to reduce fringing in the red. The instrument saw first light on the DCT in the spring of 2015, and was in regular operation within a month of the first mounting. To improve the efficiency of operations of the DeVeny, we are in the process of retrofitting motors to the grating tilt mechanism, the collimator focus and the slit width controls. The upgrade effort has been led by T. Bida, with assistance from many of the Lowell Observatory instrument staff.

The most recently installed instrument is the Near IR High Throughput Spectrograph (NIHTS).[4] NIHTS covers roughly 0.9 to 2.4μm in one exposure at an average resolution of 160. This effort has been led by H. Roe. The instrument was assembled in the Lowell shop in late 2015, and saw first light on the DCT at the end of November 2015. It is still in the process of being commissioned, with the expectation that it will go into regular science operations in late 2016. NIHTS is mounted on one of the folded ports of the RC instrument cube. The long term plan is to fold the beam to it using a dichroic, permitting simultaneous near IR spectroscopy with NIHTS and optical imaging with LMI. Initial testing has been done with a fold mirror with a standard bare aluminum coating.

2.2 Visiting Instruments – POETS and DSSI

In addition to the planned first generation instruments, DCT has also hosted two instruments, POETS and DSSI. These bring high spatial and temporal resolution capability to the facility. They were also useful in commissioning the DCT.

POETS (Portable Occultation, Eclipse and Transit System; see Ref. 5) is a portable high speed imaging system designed for observing stellar occultations. With the addition of a commercial focuser and a two-inch adapter, it was straightforward to mount POETS. In addition to observations of possible occultations by solar system bodies, it has also been used to help assess the performance of the telescope systems.

The Differential Speckle Survey Instrument (DSSI; Ref. 6) built by Elliott Horch (Southern Conn. St. Univ.) has been available for use at DCT when it is not being used at Gemini and WIYN. Typically it has been used for a week per quarter during bright time. It is capable of reaching down to V = 14 mag on the DCT, with spatial resolution ~ 70 milliarcsec, which is about twice the diffraction limit of the telescope.

2.3 Upcoming Instruments – IGRINS, RIMAS, and EXPRES

In addition to the current instruments, there are three instruments that are expected to go into use at the DCT over the next six months to two years, and significantly expand the capability of the facility. The instruments are IGRINS, RIMAS and EXPRES.

The Immersion Grating Infrared Spectrometer (IGRINS)[7,8] is currently in use at McDonald Observatory.[9] This was designed and built by a team from UT Austin and KASI. Work has begun to make it possible to mount it on the DCT for up to six months a year for the next several years. Beginning in late 2016, this will bring high resolution near IR spectrographic capability to the DCT in a tested and superbly functioning instrument.

The Rapid Infrared Imager-Spectrometer (RIMAS) is a dual beam near infrared imager-spectrometer being built at the Goddard Space Flight Center for use on the DCT.[10] Progress on RIMAS is presented at this meeting (see presentations Refs. 10–12). RIMAS is projected to be installed on the DCT in late 2016 or early 2017. The imaging field of view will be about $3'$, and the spectrometer side will support low and medium resolution.

The extreme precision spectrograph (EXPRES) is being built at the Yale Exo-Planet Laboratory, and will undertake a large survey for Earth mass planets once it is installed on the DCT in mid-2017.[13] This will be a fiber fed, bench mounted spectrograph capable of providing resolution above R $\sim 100,000$.

3. IMAGE QUALITY EXPECTATIONS

Now that DCT is in regular operations, we wanted to assess how well the full system has done in meeting image quality goals, and to evaluate how the actual seeing has compared with the site testing measurements. The two most pertinent question are:

1. How does the image quality compare to what was expected from the site testing?

2. What does the image quality look like in a typical science image?

3.1 Expectations from Site Testing

The astronomical seeing and environmental characteristics of the DCT site at Happy Jack, AZ were tested between January 2003 and May 2004.[14] The site seeing was evaluated using a DIMM system on 117 nights during the period. The site testing showed that for an assumed effective wavelength of 0.7μm that the median site seeing was $0.''84$, the mean was $0.''90 \pm 0.22$, the modal bin was centered at $0.''75$ and the first quartile was $0.''62$ (see Fig. 1, which is Fig. 3 in Ref. 14). The site testing measurements were all corrected to zenith pointing, assuming a Kolmogorov type turbulence model, with $\cos^{-3/5}(z)$ dependence on the zenith distance z.[14]

3.2 Delivered Image Quality Budget

The top level system requirements for the RC focus of the DCT[15] specified that the local contributions to the seeing should not degrade the atmospheric seeing measured on site by more than 10% and 25% of the first quartile value in closed- and open-loop modes respectively.[16,17] For a first quartile of $0.''62$, the maximum degradation budgeted for the telescope and local seeing contribution works out to be $< 0.''28$ over a $15' \times 15'$ field of view at the RC focus. This specification assumes closed loop correction. This was relaxed to ΔFWHM $< 0.''47$ for the open loop case when no guide or wavefront stars are available. The image size requirement was relaxed proportional to $\cos^{-3/5}(z)$, allowing the image size to grow with atmospheric seeing, but keeping the fractional local contributions the same. Table 1 lists the site survey data, the total FWHM including the projected contributions from the telescope and local site at the zenith, and the corrected and near zenith samples of FWHM data from 2015. It also shows the computed local site and telescope contributions to the seeing for the measured 2015 FWHM data, presuming the site testing data indicate the free atmosphere contribution.
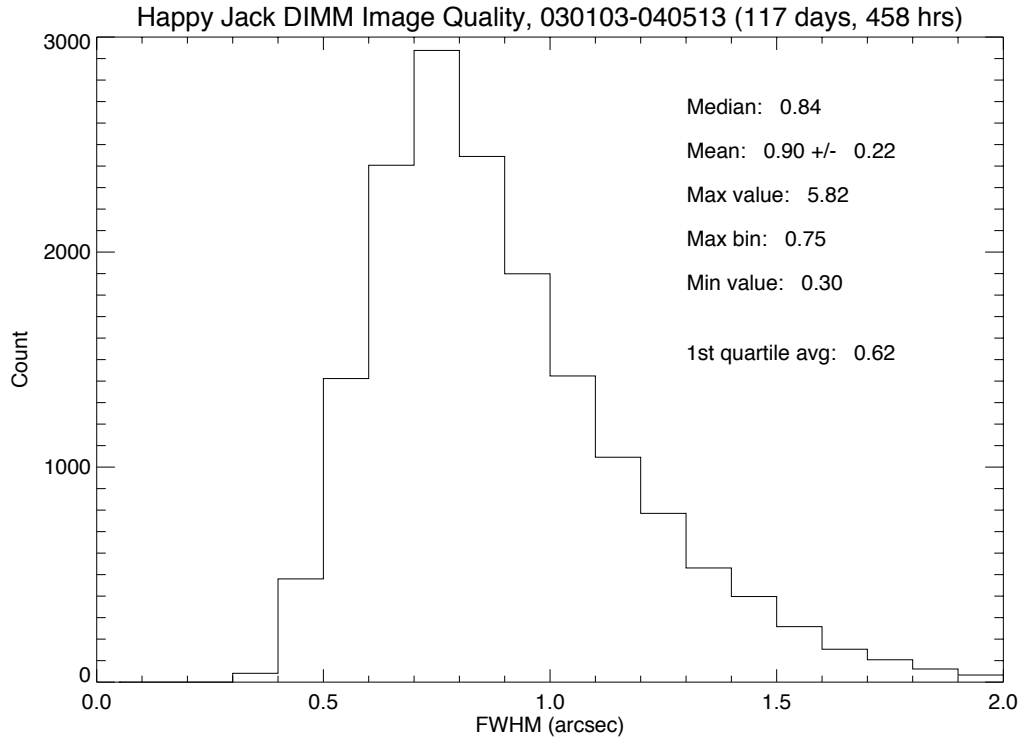
Figure 1. The histogram of seeing measurements made with the Lowell DIMM during site testing at Happy Jack, between 2003 Jan 03 and 2004 May 13.(Ref 14, Fig. 3.)

3.3 The Active Optics System and the Wavefront Open Loop Model

The control of the Active Optics System (AOS) for the DCT is designed to maintain the figure of the primary mirror and the collimation of the primary and secondary mirrors as the temperature and zenith angle of the telescope change.[18,19] The system includes a Shack-Hartmann wavefront sensor in the RC instrument cube, which can provide feedback to the control system. Over a period of roughly 18 months, as part of the commissioning process, wavefront data were gathered as a function of pointing and temperature and used to construct an open loop model (referred to as the WOLM, or Wavefront Open Loop Model) for the low order aberration terms.[2,19] Once that was implemented, that model has been used for all normal operations. The AOS and the WOLM are critical for the DCT to live up to its design potential.

3.4 Early Delivered Image Quality (pre-WOLM installation)

Before we had enough data to construct the WOLM, the primary mirror support model assumed a uniform distribution of the mass of the mirror over the supports. This was our initial model, and is still used when collecting additional data to improve the WOLM.

With the uniform model, the FWHM measured on images taken early in the commissioning process in 2012 was typically between 0.″9 and 1.″1 without any wavefront correction in a modest field on-axis. Correcting for Zernikes 4 through 11 (focus, coma, astigmatism, trefoil and spherical) improved the FWHM to between 0.″8 and 1.″0.[1] This amounted to correcting between roughly 0.″4 and 0.″7 worth of aberration, when removed in quadrature. Fig. 2 is from Ref. 1 and shows a sample uncorrected and a manually corrected stellar image, and the corresponding radial profiles.

Table 1. The distribution of FWHM at Zenith. The values measured with a DIMM setup during the site testing are in column 2. The DCT top level requirements specify that the telescope and local seeing contributions will not degrade the site seeing by more than 10% and 25% in closed and open loop mode (columns 3 & 4). The measured image FWHM data from 2015 are in columns 5, 6 & 7. Column 5 shows the raw FWHMM converted to equivalent FWHM($z = 0$). Column 6 is the raw FWHM for images taken within 15° of zenith and column 7 shows the intercept when fitting a $\cos^{-3/5}(z)$ law to the raw FWHM data. The contribution to the 2015 measured FWHM from the local site and telescope are computed below the 2015 data in columns 5, 6 & 7.

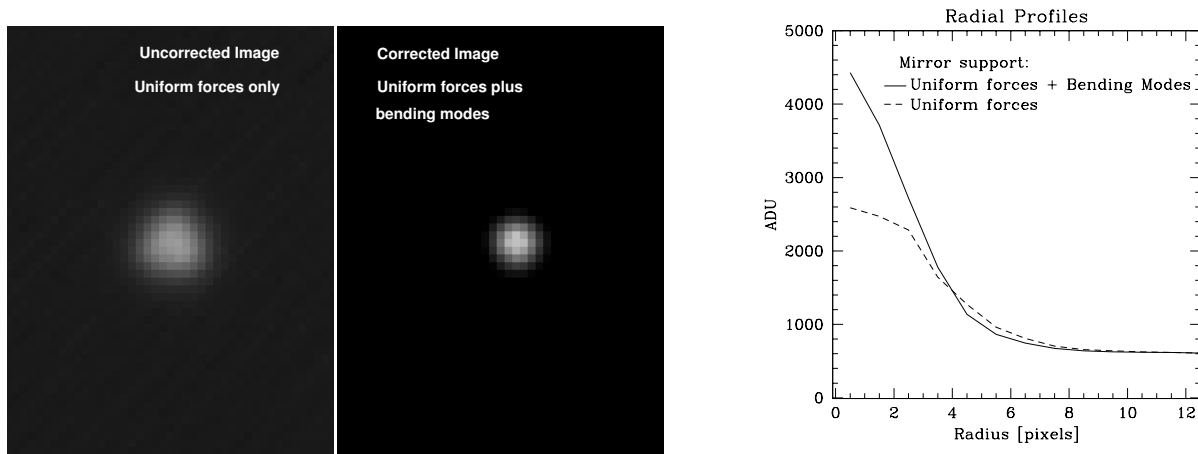|	Measured Atmospheric FWHM[14]	Local & Telescope Contribution		2015 Image FWHM Data		
		Closed Loop[15] 0″28	Open Loop[15] 0″47	corrected to $z = 0$	raw for $0 \leq z < 15°$	$\cos^{-3/5}$ fit for FWHM($z = 0$)
1st Quartile	0″62	0″68	0″78	0″74	0″71	
Mode	0″75	0″80	0″89	0″75	0″65	
Median	0″84	0″89	0″96	0″93	0″90	0″93
Mean	0″90	0″94	1″02	1″04	1″03	
Computed Local & Telescope Contribution						
1st Quartile				0″40	0″35	
Mode				⋯	⋯	
Median				0″40	0″32	0″40
Mean				0″52	0″50	

Figure 2. Stellar images taken with the prime focus test array with the primary mirror uniformly supported (left) and with corrective bending modes applied (middle). The radial profiles from the two stellar images show noticeable improvement when the mirror is bent to correct for aberrations (right). (Ref. 1, Fig. 8.)

In a similar vein, we made an initial simple assessment of the image quality off axis. We found that PSF for images in the center and corners of the the first camera (borrowed from the Lowell 42-inch) and later the LMI were visually very similar.[1,2]

3.5 The Wavefront Open Loop Model

As soon as we had a functional wavefront sensor, we began collecting data to use in the construction of the open loop model. The basic process was described in Ref. 19. We took data with the optics in the nominal,

uniform configuration at varying zenith angles, over a range of temperatures. The whole process took roughly 18 months, primarily so that we could cover a wide enough range in temperature and get enough data for decent statistics. WOLM data collection started in 2012, with major work in 2013 and 2014; the coefficients for the current WOLM were given in Ref. 2. As opportunity allows, we continue to collect WOLM data to refine and verify the status of the existing model. As will be seen below, we have been able to determine a correction to the temperature coefficient for the focus term from the scientific imaging data. The current version of the WOLM was put into service on 13 November 2013, and has been in use for all observing since, with the exception of data collected specifically for WOLM and pointing model updates.

4. DELIVERED IMAGE QUALITY IN 2015

As noted above, from Refs. 15, 16, 19, the nominal contribution to the FWHM from the facility needs to be less than $0.''47$ or $0.''28$ to meet respectively the open loop and closed loop image quality requirements.

We have reduced the ensemble of image data acquired during 2015 using the LMI. Most of these data were taken for science projects, with a modest fraction taken in support of engineering work. In 2015, parts of 293 nights were scheduled for science observations. We have at least minimal data from 228 nights. Of those, 210, 196 and 163 nights have respectively at least 10, 20 and 50 images where we were able to measure stellar profiles. Along with the measured image profiles, the image headers provide needed supporting information, including pointing data (zenith distance and azimuth), environmental data (ambient and mount temperatures, wind direction and velocity) and exposure data (UT, exposure time, etc.).

All the images were bias and flat corrected. Sextractor[20] was used to detect objects and measure their position and FWHM using a two dimensional circular Gaussian model. Objects which were flagged as possibly blended were removed from the sample. The mean, median and mode of the FWHM measurements within each image were tabulated. From that list for each night, we also computed the nightly mean image median FWHM. For the statistics on a night-by-night basis, we used the mean median. For statistics based on the individual images, we used the computed image medians.

The statistics presented are all based upon data taken for a diverse set of projects, and hence are not necessarily consistently sampled in time or environmental conditions. Each observer has their own particular criteria for what constitutes usable conditions, and ways of deciding on best focus. The images are taken through most of the filters currently in use with LMI, driven entirely by the demands of the observers' scientific programs. It is also worth noting how the DCT normally operates. The WOLM runs all the time. At the start of the night, the TOs will tune the telescope optics manually; they take a series of wavefront measurements and correct the residual aberrations not removed by the WOLM. Most observers tweak the focus at that time. After that, additional tuning of the optics is at the discretion of the observer. Typically, most people do not re-tune more than once or twice a night. This means that for the bulk of these data, the WOLM is the primary correction mechanism, with an initial zero point correction done at the start of the night.

4.1 Environmental Statistics

Environmental data are included in each FITS image header. They are recorded at the time the shutter opened for the exposure. Fig. 3 shows the average night time wind speed (upper left), average night time ambient temperature (lower left) and night time range in temperature (lower right). A minimum of five science images was set as a lower cut-off for computing the nightly averages and range. The upper right plot of Fig. 3 is a polar plot showing the overall distribution of wind velocity as a function of wind direction. The black points are the data from each individual frame. Those were sorted in direction, binned by 100 and the median of the bins computed. Those medians are plotted as red squares.

The prevailing winds are from the West, followed by the East. The wind velocity frequency peaks between 2 and 3 m/s (see Figs. 6 and 7). The range in night time temperatures is typically below 5°C. The temperature measurements only come from science images, not including twilight biases and flats, and so are more representative of the overall fluctuations at the site during the night.
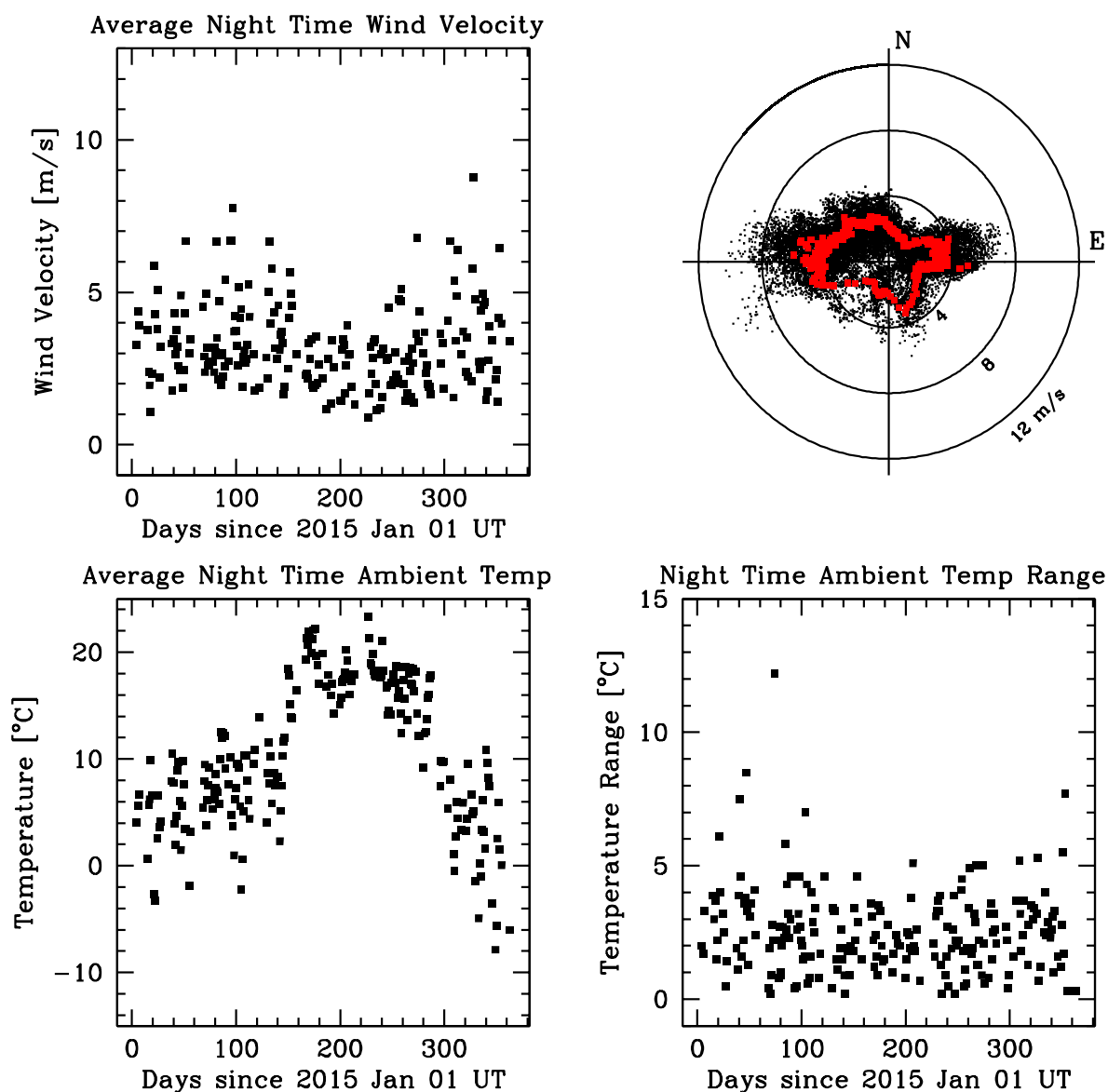
Figure 3. All the weather statistics given here are taken from image headers; they represent the state of the DCT when it was open for observation. *Upper left:* The average night time wind velocity for each night in 2015. *Lower left:* The average night time temperature, as recorded by the site weather station. *Upper right:* The distribution of wind velocity versus wind direction. The black points are the individual velocity and direction values from each image. The values were sorted in direction, and the red squares are the median values of sets of 100 velocity and direction pairs. The concentric rings are at wind velocities of 4, 8 and 12 m/s. *Lower right:* The differences between the night time high and low temperatures.

4.2 FWHM vs Zenith Distance

In Fig. 4, the image FWHM data are plotted versus the zenith distance at which the image was taken. Because of the large variation in conditions from night to night, we sorted the data in zenith distance and then binned the data two ways to increase the signal to noise. The black points are the median FWHM of all the images

within each 15 degree wide bin of zenith distance. The number of images within each bin is given along the bottom of the figure. The error bars indicate the 1st and 3rd quartile FWHM for each bin. The red points were computed by taking the median value of each set of 500 images in zenith distance order.

To the red points, we fitted both a linear model and a $\cos^{-3/5}(z)$ model. The data above zenith angle of $65°$ are reasonably well fit by a straight line approximation. The FWHM degrades at about $\Delta \mathrm{FWHM}/\Delta z \approx 0\rlap{.}''009$/degree. The cos fit was done under the assumption that the seeing would degrade based on a Kolmogorov type turbulence model. The one fit coefficient is an estimator of the median FWHM at zenith, and in this case is $\mathrm{FWHM}(z = 0) \approx 0\rlap{.}''93$.

We also evaluated the image FWHM data by looking at the ensemble median and quartiles. The upper panel (a) of Fig. 5 shows the raw distribution of image FWHM for all images. The middle panel (b) shows the distribution for the entire ensemble after correcting by $\cos^{-3/5}(z)$ (the "corrected set"), and the lower panel shows the uncorrected distribution for the images taken near the zenith. This last set (the "zenith sample") should be a good sample of the real performance for comparison with the site testing data. The distribution of FWHMs for the corrected set and the zenith sample show very much the same characteristics, and very similar population measures (median, etc.). The median also agrees well with the median FWHM at $z = 0$ based on the fit to the median binned data as a function of z. (See Table 1 for a compilation of the various estimators of the $\mathrm{FWHM}(z = 0)$.)

The answers to the two questions posed at the beginning of section 3 are similar. The science image data quality has a median FWHM of about $0\rlap{.}''93$, and a first quartile of about $0\rlap{.}''74$. These numbers are in line with what was hoped and predicted from the site testing data and the DCT top level requirements. In fact, we found that the system operates slightly better than required in open loop mode. The nominal computed contribution from the telescope and local facilities is roughly $0\rlap{.}''40$, which is noticeably better than the budgeted $0\rlap{.}''47$. If the zenith sample is more representative, then the facility contribution shrinks to $0\rlap{.}''34$. The mean FWHM data are slightly worse, though still in line with the original DCT top level requirements. This is likely a reflection of a couple of things: the inclusion of measurements of non-stellar objects in the data set, and the inclusion of engineering data, both of which would be likely to add to the large FWHM tail of the distribution.

4.3 FWHM vs Wind

We found a modest degradation of the image FWHM as the wind speed increases (see Fig. 6). Initially, it appeared that the fall-off was more pronounced at larger zenith distance, but almost all of the difference can be attributed to the expected fall-off due to turbulence as a function of zenith distance. This helps validate the assumption in the DCT top level requirements that the site and telescope contribution would relax as $\cos^{-3/5}(z)$. We also see that the best seeing is realized when the wind speeds are between 2 and 4 m/s. The seeing degrades at roughly $\Delta \mathrm{FWHM}/\Delta v \approx 0\rlap{.}''10\,/(\mathrm{m/s})$.

The dependence of the FWHM on the wind direction showed two things (see Fig. 7). First, most images were taken with the wind out of either the West or the East; the prevalance of East/West becomes stronger at higher wind speeds. Secondly, the median FWHM when the wind is out of the West is very similar between the low ($0 \leq v < 3\,\mathrm{m/s}$) and moderate ($3 \leq v < 6\,\mathrm{m/s}$) cases. When the wind is from the East, the FWHM is significantly larger when the wind speed is higher.

4.4 FWHM vs Time

We looked briefly at the distribution of image FWHM as a function of image exposure time. This is harder to quantify, since several effects are likely to be correlated. For example, when the seeing is poorer, exposures will be longer to reach desired signal-to-noise levels. Fig. 8 shows the distribution of FWHM for three ranges of exposure times t: $0 < t \leq 10\,\mathrm{sec}$, $10 < t \leq 30\,\mathrm{sec}$, and $120 < t \leq 240\,\mathrm{sec}$. The raw FWHM distributions are shown in the left column, and the distributions corrected to $z = 0$ are in the right. After correction, the distributions show slight degradation with increasing exposure time. At this point, the effect is small enough that we have not drawn any conclusions from this.
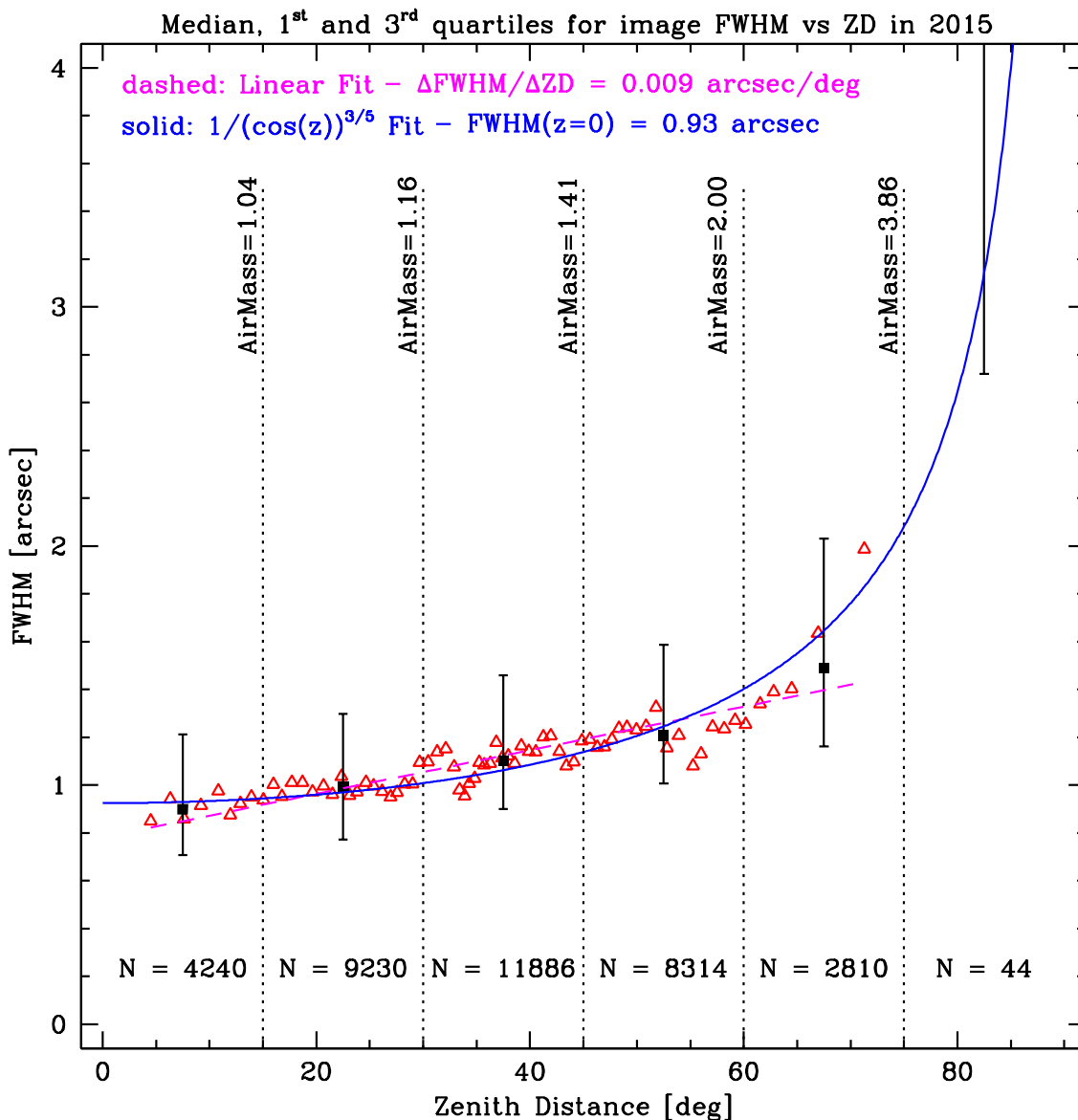
Figure 4. The ensemble of image median FWHM measurements were sorted in zenith distance. The median and 1st and 3rd quartiles were computed for the set of measurements within each $15°$ bin. The black points mark the median FWHM, and the lower and upper error bars mark the 1st and 3rd quartile FWHMs. The red points are median FWHM values for 500 images. The dashed magenta curve is a linear fit to the red points. The slope is a reasonable approximation to the degradation of the image quality for $z \leq 65°$. The solid blue curve is a fit for $\mathrm{FWHM}(z) = \mathrm{FWHM}(z = 0) \times \cos^{-3/5}(z)$. The fitted coefficient $\mathrm{FWHM}(z = 0) = 0.''93$ is an estimate of the median FWHM at zenith.

5. UPDATING THE WOLM

Given the critical nature of the WOLM to maintaining good image quality, we are always looking for ways to improve it. The focus term is the most sensitive to changes in temperature, since it is determined largely by the spacing between the primary and secondary mirrors. For each filter, we have measured a zero point shift from
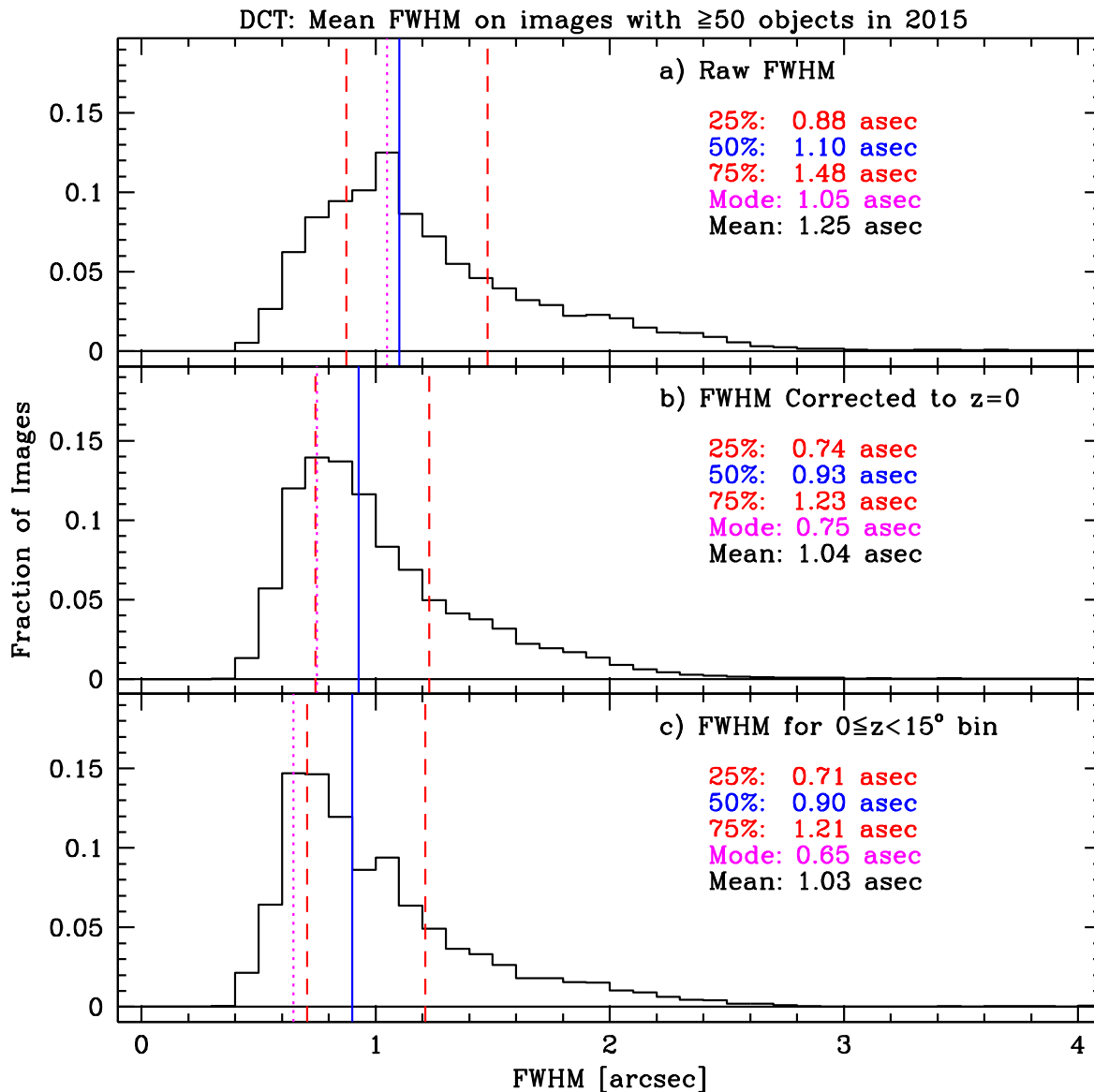
Figure 5. The distribution of FWHM for images with at least 50 objects for which we could measure a FWHM. The upper panel (a) shows the raw distribution of FWHM for all images taken during 2015. In the middle panel (b), the FWHMs have been corrected for atmospheric turbulence by a factor of $\cos^{-3/5}(z)$, making them all estimates for the FWHM at $z = 0$. The lower panel (c) shows the distribution of FWHM for those images that were actually taken up near the zenith, in the range $0 \leq z < 15°$. The solid blue line marks the median, the dashed red lines the quartiles and the dotted magenta line the mode of each histogram.

the nominal focus curve to account for the optical construction of the filter; we call that the focus offset. Part of most observers' normal routine is to check the focus at the beginning of the night, after the optics have been tuned up by the TO, and tweak the nominal focus offset. Because of this, we have a built in way to refine the focus offset versus temperature coefficient, assuming most observers have similar ideas about what constitutes good focus.
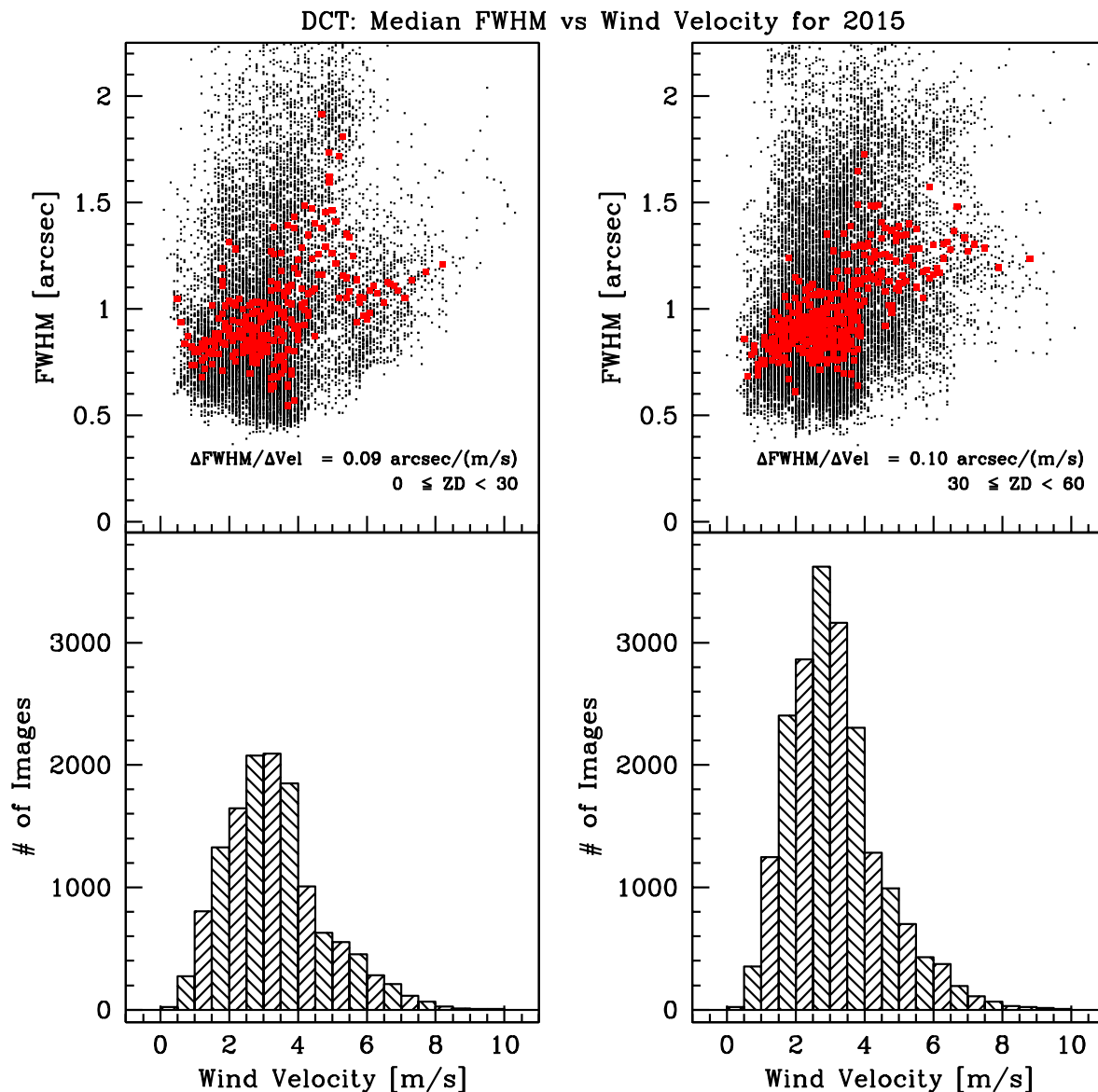
DCT: Median FWHM vs Wind Velocity for 2015

ΔFWHM/ΔVel = 0.09 arcsec/(m/s)
0 ≤ ZD < 30

ΔFWHM/ΔVel = 0.10 arcsec/(m/s)
30 ≤ ZD < 60

Figure 6. FWHM corrected to $z = 0$ vs wind velocity. The distributions have been split into high ($0 \leq z < 30°$, left column) and middle/low elevation ($30 \leq z < 60°$, right column). The individual image FWHMs are plotted in black. The red points are the medians of sets of 50, sorted by wind velocity.

In Fig. 9, we have plotted up the recorded values of focus offset versus mount temperature for images in V and R taken over the course of 2015 (black points). We limited the images to those with measured FWHM $\leq 1''25$. This was chosen to balance good image quality versus coverage in temperature. These were sorted in mount temperature, and then we computed the median value of each sequential set of 25 (red triangles). To the medians, we fit a line. The slope of the line is the amount by which we need to modify the focus temperature coefficient to improve the focus following as a function of temperature. As can be seen, the nominal change in slope is about $4.7 \, \mu\text{m}/°\text{C}$ change in the position of the secondary relative to the primary mirror as a function
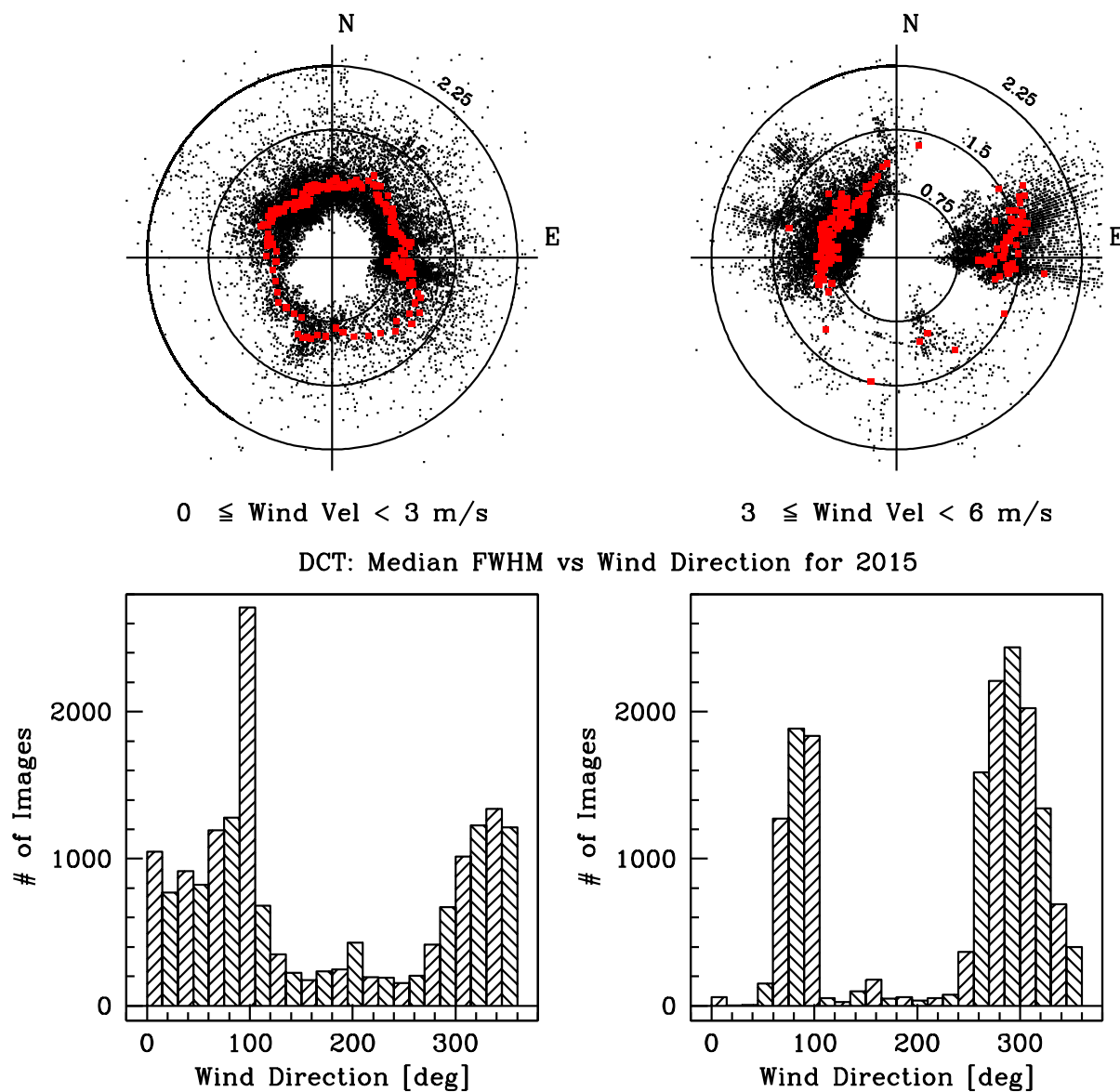
Figure 7. FWHM corrected to $z = 0$ vs wind direction, split into low ($0 \leq v < 3\,\mathrm{m/s}$, left) and moderate ($3 \leq v < 6\,\mathrm{m/s}$, right) wind speed conditions. The black points are the individual image median FWHM. The red squares are the median values for bins of 100 measurements. On the upper plots, the concentric rings are FWHM = $0''\!.75$, $1''\!.50$, & $2''\!.25$.

of temperature. Within the uncertainties, the slope was independent of color. Converting the WOLM focus temperature coefficient (referred to as Z4 kMT in Ref. 2) to equivalent units we find the desired change in slope is about 6.8%.
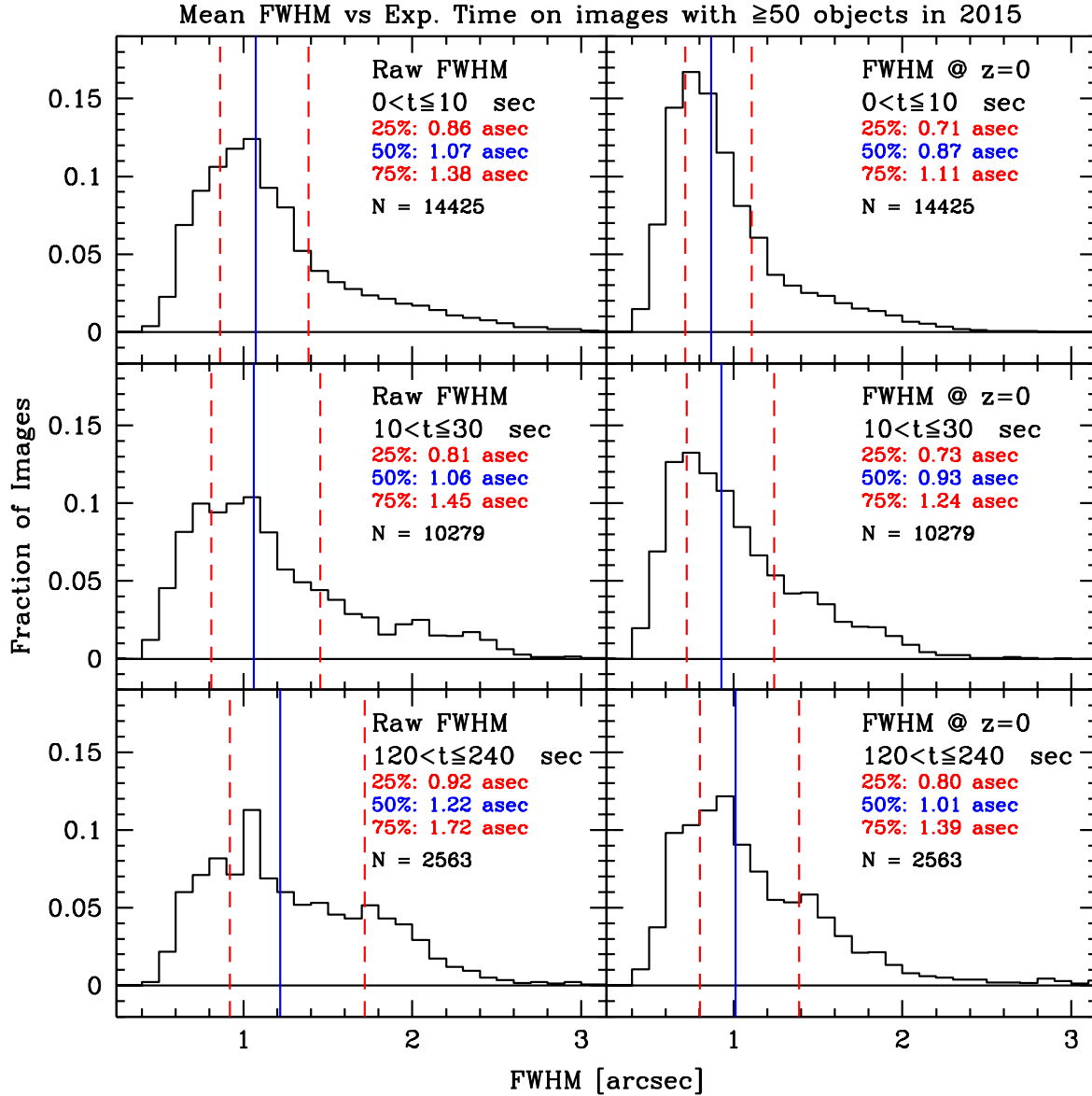
Figure 8. The distribution of FWHM for images with at least 50 objects for which we could measure a FWHM versus exposure time. The left column shows the raw FWHM measurements. FWHM measurements in the right hand column have been corrected for atmospheric turbulence by a factor of $\cos^{-3/5}(z)$, making them all estimates for the FWHM at $z = 0$. Three groups of exposure times (t) are shown. *Top row:* Images with $0 < t \leq 10$ sec. *Middle row:* Images with $10 < t \leq 30$ sec. *Bottom row:* Images with $120 < t \leq 240$ sec. The solid blue line marks the median of each distribution. The dashed red lines the 1st and 3rd quartiles. N is the number of images in each time bin.

6. CONCLUSIONS

During the summer of 2016, we will be re-aluminizing the primary mirror for the first time, so this was a good time to review the performance of the DCT, and think about the next steps. We found that the system is
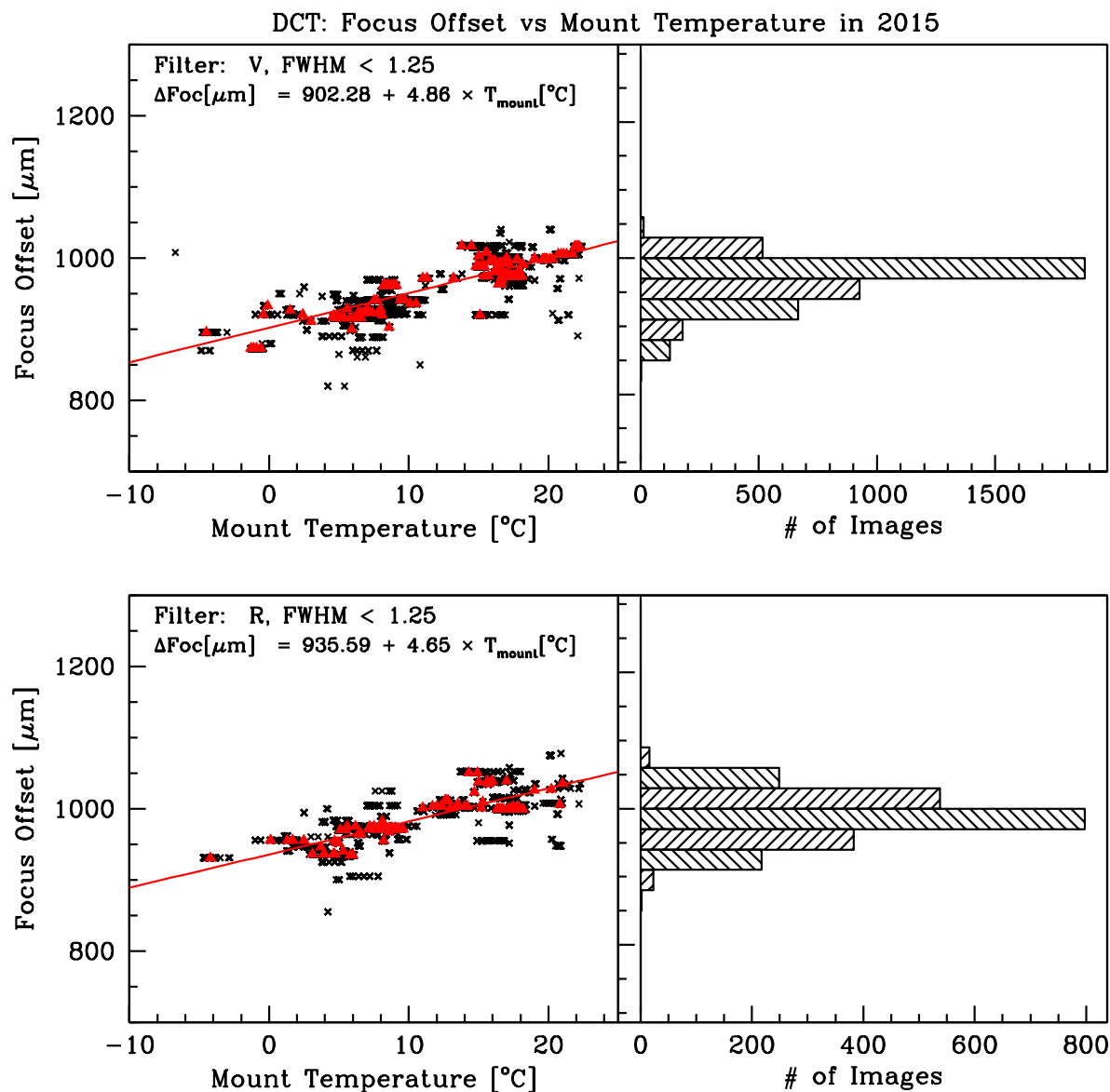
Figure 9. Focus offset versus mount temperature. The focus offset is the displacement from the separation between M1–M2 predicted by the WOLM. For images in V (upper panel) and R (lower panel), we have plotted the actual focus offset used. The black points are the focus offsets from the individual images, and the red triangles are medians of 25, sorted by temperature. The red line is a linear fit to the offset vs temperature.

performing at or better than the open loop design specifications for delivered image quality and that the FWHM degrades as expected as a function of zenith distance.

From the data gathered during 2015, we have learned the following:

1. The median and 1st quartile seeing at zenith in 2015 were 0″.93 and 0″.74 respectively.

2. The nominal computed contribution to the seeing from the telescope and site in 2015 was $0.''40$, which is better than the requirement of $< 0.''47$.

3. The FWHM degrades with increasing wind speed as $\Delta\text{FWHM}/\Delta v \approx 0.''10/(\text{m/s})$.

4. The best seeing typically occurs with wind speeds between 2 and 4 m/s.

5. The seeing tends to be more consistent and better when the wind comes from the West.

6. The WOLM focus temperature coefficient can be improved by about 6%.

Looking forward, after we re-coat the primary mirror, there are a couple of things that we will be working on:

1. The integration of several new instruments (IGRINS, RIMAS and EXPRES) over the next two years will greatly expand the capabilities of the facility.

2. The next logical step in improving the image quality will be to implement closed loop correction to the AOS from the wavefront sensor.

ACKNOWLEDGMENTS

REFERENCES

[1] Levine, S. E., Bida, T. A., Chylek, T., et al., Status and performance of the Discovery Channel Telescope during commissioning, Proc. SPIE, 8444, 844419 15pp. (2012)

[2] DeGroff, W. T., Levine, S. E., Bida, T. A., et al., Status and performance of the Discovery Channel Telescope from commissioning into early science operations, Proc. SPIE, 9145, 91452C 18pp. (2014)

[3] Bida, T. A., Dunham, E. W., Nye, R. A., et al., Design, development, and testing of the DCT Cassegrain instrument support assembly, Proc. SPIE, 8444, 844451 16pp. (2012)

[4] Bida, T. A., Dunham, E. W., Massey, P., Roe, H. G., First-generation instrumentation for the Discovery Channel Telescope, Proc. SPIE, 9147, 91472N 11pp. (2014)

[5] Souza, S. P., Babcock, B. A., Pasachoff, et al., POETS: Portable Occultation, Eclipse, and Transit System, PASP, 118, 1550–1557 (2006)

[6] Horch, E. P., Veillette, D. R., Baena Gallé, R., et al., Observations of Binary Stars with the Differential Speckle Survey Instrument. I. Instrument Description and First Results, AJ, 137, 5057–5067 (2009)

[7] Yuk, I.-S., Jaffe, D. T., Barnes, S., et al., Preliminary design of IGRINS (Immersion GRating INfrared Spectrograph), Proc. SPIE, 7735, 77351M (2010)

[8] Park, C., Jaffe, D. T., Yuk, I.-S., et al., Design and early performance of IGRINS (Immersion Grating Infrared Spectrometer), Proc. SPIE, 9147, 91471D 12pp. (2014)

[9] Mace, G., Kim, H., Jaffe, D. T., et al., 300 nights of science with IGRINS at McDonald Observatory, Proc. SPIE, 9908, 9908-11 (this meeting) (2016)

[10] Kutyrev, A. S., Toy, V. L., Capone, J. I., et al., RIMAS: Infrared imager-spectrometer for the Discovery Channel Telescope, Proc. SPIE, 9908, 9908-208 (this meeting) (2016)

[11] Toy, V. L., Kutyrev, A. S., Capone, J. I., et al., HXRG detector characterization for RIMAS and instrument efficiencies, Proc. SPIE, 9908, 9908-131 (this meeting) (2016)

[12] Kuzmenko, P. J., Little, S. L., Kutyrev, A. S., Capone, J. I., Diamond machining of large ZnSe grisms for the Rapid Infrared/Imager Spectrograph (RIMAS), Proc. SPIE, 9912, 9912-11 (this meeting) (2016)

[13] Jurgenson, C. A., Fischer, D. A., McCracken, T. M., et al., EXPRES: a next generation RV spectrograph in the search for earth-like worlds, Proc. SPIE, 9908, 9908-258 (this meeting) (2016)

[14] Bida, T. A., Dunham, E. W., Bright, L. P, Corson, C., Site testing for the Discovery Channel Telescope, Proc. SPIE, 5489, 196-206 (2004)

[15] Smith, B., Top-Level Telescope and Facility Requirements, DCT-0000S-002-5, 18pp. (2009)

[16] Smith, B., Manuel, A., Delivered image quality budget for the Discovery Channel Telescope, Proc. SPIE, 7738, 773805 20pp. (2010)

[17] Smith, B., Delivered Image Quality Budget, DCT-0810A-001-6, 52pp. (2011)

[18] Smith, B., Chylek, T., Cuerden, B., Degroff, B., Lotz, P. J., Venetiou, A., The active optics system for the Discovery Channel Telescope, Proc. SPIE, 7739, 77391T 21pp. (2010)

[19] Venetiou, A. J., Bida, T. A., Discovery Channel Telescope Active Optics System Early Integration and Test, Proc. SPIE, 8444, 84441E 11pp. (2012)

[20] Bertin, E., Arnouts, S., SExtractor: Software for source extraction, A&A Supp., 317, 393–404 (1996)